조선대학교 CHOSUN UNIVERSITY

2016年 2月

碩士學位 論文

2016年 2月 碩士學位論文

Surface Characteristics of HA and Zn-HA Coatings on the Nanotubular Ti-xNb Alloys by Electrochemical Deposition Method

Surface Characteristics of HA and Zn-HA Coatings on the Nanotubular Ti-xNb Alloys by Electrochemical Deposition Method

朝 鮮 大 學 校　大 學 院

光技術工學科(光應用工學專攻)

邊　仁　燮

Surface Characteristics of HA and Zn-HA Coatings on the Nanotubular Ti-xNb Alloys by Electrochemical Deposition Method

나노튜브 형성된 Ti-xNb 합금표면에 전기화학적
방법으로 석출된 HA 및 Zn-HA막의 표면특성

2016年 2月 25日

朝鮮大學校 大學院

光技術工學科(光應用工學專攻)

邊 仁 燮

Surface Characteristics of HA and Zn-HA Coatings on the Nanotubular Ti-xNb Alloys by Electrochemical Deposition Method

指 導 敎 授   崔 漢 喆

이 論文을 工學 碩士學位申請 論文으로 提出함

2015年 10月

朝鮮大學校 大學院

光技術工學科(光應用工學專攻)

邊 仁 爕

邊仁燮의 碩士學位論文을 認准함

委 員 張　朝鮮大學校　　　教　授　　孫 美 敬　印

委　　員　朝鮮大學校　　　教　授　　金 炳 勳　印

委　　員　朝鮮大學校　　　教　授　　崔 漢 喆　印

2015年　11月

朝 鮮 大 學 校　大 學 院

CONTENTS

LIST OF TABLES

LIST OF FIGURES

국 문 초 록

나노튜브 형성된 Ti-xNb 합금표면에 전기화학적 방법으로 석출된 HA 및 Zn-HA막의 표면특성

변 인 섭
지도교수: 최한철, 공학/치의학박사
광기술공학과 (광응용공학전공)
조선대학교 대학원

최근 상업적으로 많이 사용되어지고 있는 티타늄 합금은 좋은 기계적 특성 및 부식저항성, 우수한 생체적합성 때문에 본 플레이트, 인공관절, 치과용 임플란트 등과 같은 생체재료로 널리 쓰이고 있다. 본 논문에서는 현재 사용되고 있는 Ti-6Al-4V 합금의 Al원소와 V원소의 인체에 영향을 끼치는 독성문제를 해결할 수 있으며, 저탄성계수인 Ti-xNb 이원계 합금을 개발하였고, Nb 함량을 10, 30 및 50 wt.% 가 되도록 변수를 주었으며, 아크용해법을 이용하여 합금을 설계하였다. 제조된 합금은 1000℃에서 12시간동안 열처리한 후 급냉하는 방식으로 시편을 준비하였다. 코팅 처리하지 않은 Ti-xNb 합금 표면에 수산화인회석 (HA)과 아연 (Zn)를 전기화학적 방법으로 코팅하였고, 1 M H_3PO_4 용액과 0.8 wt.% NaF 를 첨가한 전해질 용액에서 양극산화 방법으로 30 V 에서 1시간 동안 샘플 표면에 나노스케일의 튜브를 형성한 후, 나노튜브 표면에 HA와 Zn를 전기화학적 방법으로 코팅을 하였다.

두 단계로 처리된 Ti-xNb 합금의 표면특성은 광학현미경, 주사전자현미경, EDS 및 X-선 회절분석기를 사용하여 분석하였다. 코팅 처리하지 않은 Ti-xNb 합금 표면에 HA 와 Zn를 코팅한 샘플과 나노튜브를 형성 후 코팅한 Ti-xNb 합금 표면의 특성을 분석하여 다음과 같은 결과를 얻었다.

1. 광학현미경 분석 결과, Ti-10Nb 합금의 미세구조는 주로 침상구조가 관찰되었으나, Nb 함량이 증가할수록 Ti-30Nb 합금 에서는 침상구조와 등축정 구조가

같이 나타났으며, Ti-50Nb 합금 에서는 대부분 등축구조로 되어있었다. X-선 회절분석 결과 Ti-10Nb 합금 에서는 주로 α"피크를 보였으며 Nb 함량이 증가할수록 α"의 피크가 감소하고. β상의 피크가 증가하였다.

2. Ti-10Nb, Ti-30Nb 및 Ti-50Nb합금의 나노튜브 구조는 두 가지 직경으로 구성되었고 불규칙한 분포를 보여주었다. 또한 나노튜브길이는 Nb함량이 증가함에 따라 증가하였다.

3. 합금의 수산화인회석 코팅은 나노로드 모양의 형상으로 나타났고, 수산화인회석과 아연을 코팅한 합금은 나노네트워크 형태를 보였다.

4. 나노튜브의 표면은 HA와 Zn-HA 석출물로 균일하게 덮여 졌으며 HA 석출물은 큰 판상으로 나타났고, Zn-HA는 작은 입자형태로 나노튜브 표면에 석출되었다.

5. HA를 석출한 경우는 코팅표면에서 Ca와 P가 균일하게 분포되었고 Zn-HA를 코팅한 경우에는 Ca, P, 및 Zn이 균일하게 분포되었다.

결론적으로, 생체 적합성을 갖는 Ti-xNb 합금에 나노튜브를 형성한 후, 골과 유사한 물질인 수산화인회석 코팅과 아연을 코팅처리 시 균일하게 표면이 코팅됨으로써 생체재료로 사용될 경우 골 융합성을 향상시킬 수 있을 것으로 생각된다.

Ⅰ. INTRODUCTION

Commercially pure titanium (CP-Ti) and Ti-6Al-4V alloys are the most common used as implants of orthopedics and dentistry because of their good biocompatibility, good resistance to corrosion, excellent mechanical properties, and workability [1]. Especially, the Ti-6Al-4V alloy (α + β type) is the most widely used material due to its reported that the biocompatibility and hemocompatibility result from a thin Ti dioxide-based layer that is always present on the metal surface [2]. The addition of alloying elements, such as Al and V, improved the mechanical properties of Ti [3, 4]. However, there are some problems of the alloy such as that alloy has properties of high elastic modulus and toxicity of V element and Alzherimer's disease of Al element, when compared with that of bone and potential adverse human effects. To improve the problem, new Ti alloys with nontoxic elements such as zirconium (Zr), niobium (Nb), and tantalum (Ta) elements would be recommended [5, 6]. Some researchers have focus on Ti-Nb, Ti-Ta binary system with controlling the contents of Nb, Ta elements [7]. Especially, Nb element of 4d transition metallic element is one of the most effective Ti β-stabilizer also β-stabilizer (Cp-Ti) and its alloys are the most common used as a dental implant material because of their good mechanical property, corrosion resistance and biocompatibility [8]. Furthermore, the Nb present in these alloys, a known β stabilizer reduces the modulus of the alloy and atoms of Nb occupy proprietarily the Ti sites resulting in solid-solution strengthening and precipitation hardening [9]. Therefore, the excellent characteristic of Nb are the forces driving the introduction of Ti-Nb alloys into the field of biomaterials [10]. Recently, the anodic oxidation tratment of Ti metal has attracted a great dela of attention. It is known that the protective and stable oxides on Ti surfaces are able to provide favorable osseointegration. The stability of the oxide layer depends strongly on the particular alloying element, their structure

and thickness of the film. For improvement of biocompatibility of Ti alloy, nano-scale structured surface modification is needed [11]. Also the nano-scale surface TiO_2 layer and diameter modulation of Ti alloys can be obtained function of improvement of cell adhesion, and it should be possible to control the nanotube size for biomedical implant use by controlling the applied voltage, alloying element, current density, anodization time, and electrolyte [12]. Ti and Ti alloys are generally considered to be bio-inert, and cannot bond directly to bone tissue. Therefore various surface modifications on Ti implants have been performed to improve their bioactivity. Recently Ti alloy are commonly coated with hydroxyapatite $[Ca_{10}(PO_4)_6(OH)_2, HA]$, that important to improve the cell adhesion and proliferation [13, 14]. Some of studies have been developed for HA coatings with good corrosion properties on Ti alloys for dental implant application [15]. Zinc (Zn) element play very important roles in the bone formation and immune regulations also in the most abundant trace element in bone [16, 17]. It has been demonstrated that Ti surfaces chemically modified with ZnO could significantly reduce the viability of five streptococcus bacterial strains [18]. Moreover, it can also promote bone metabolism and growth, increase bone density and prevent bone loss [19].

This electrochemical deposition is capable of deposition Zn into HA by adding Zn salt into the electrolytes. In this study, we investigated the surface characteristics of Zn-HA coated films on the nanostructured Ti-xNb alloys by electrochemical deposition.

Ⅱ. BACKGROUND

2.1. Ti alloys [20]

Ti was discovered in Cornwall, Great Britain, by William Gregor in 1791 and named by Martin Heinrich Klaproth for the Titans of Greek mythology. Ti alloys are light and have very high strength to weight ratio. They possess good biocompatibility, outstanding mechanical properties, excellent corrosion resistance and good formability. For all these reasons they are used in dental and orthopaedic applications. The metal is a dimorphic allotrope whose hexagonal alpha form changes into a body-centered cubic (lattice) β form at 882℃ (1,620°F). The specific heat of the alpha form increases dramatically as it is heated to this transition temperature but then falls and remains fairly constant for the β form regardless of temperature. The phase diagram of Ti as a function of temperature and pressure shows martensitic transformations between the α, β and ω phases. Shows transformation of Ti. Basically, Ti and Ti-based alloys can classified into α type (HCP : hexagonal-closed packed crystalline structure), near α type, β type and α+β type alloy groups (Fig. 1 and Fig. 2).
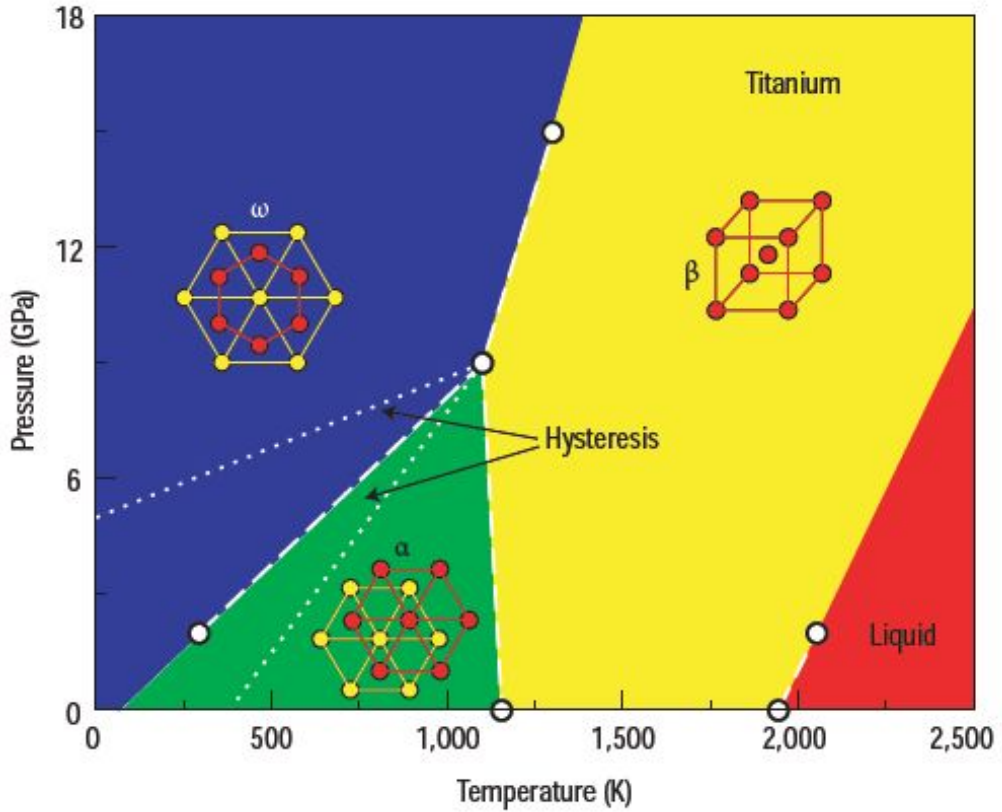
Fig. 1. The phase diagram of Ti as a function of temperature and pressure shows martensitic transformations between the α, β and ω phases [20].

Hexagonal Close Packed
HCP, α phase

Body Centred Cubic
BCC, β phase
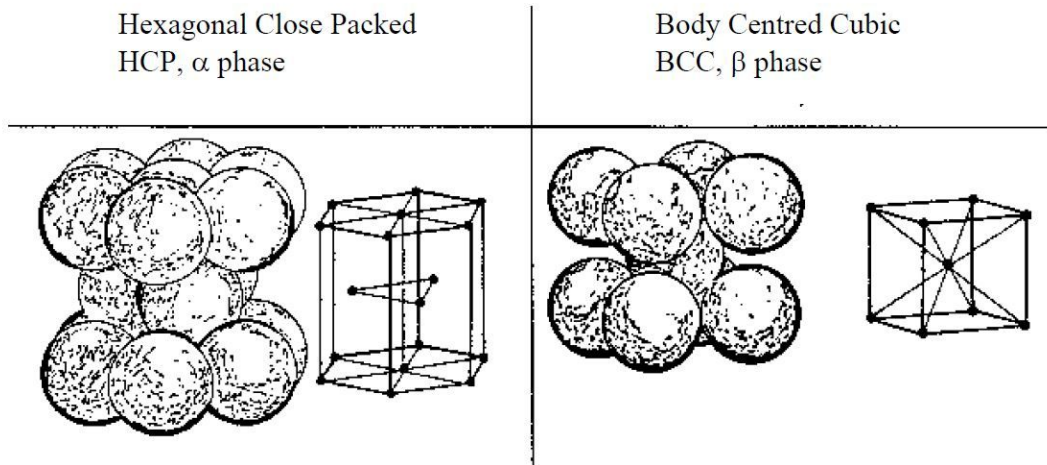
Fig. 2. The two main crystal structures of Ti [21].

2.1.1 Classification of Ti alloy [22]

Ti exists in two crystallographic forms. At room temperature, CP-Ti has a (hcp) crystal structure referred to as α-phase. At 883℃, this transforms to a (bcc) structure known as β-phase. The manipulation of these crystallographic variations through alloying additions and thermochemical processing is the basis for the development of a wide range of alloys and properties. The alloying elements have different influences on the properties of Ti. Some of the most common alloying elements and their stabilizing effect are shown in Table 1. On the other hand, elements such as nitrogen, carbon and especially oxygen have a strong α-stabilizing effect and thereby raise the α→β transition temperature (β-transus), whereas hydrogen, which has a β-stabilizing effect, lowers the transus temperature. Increasing the amount of interstitial elements leads to a drastic increase in strength (Fig. 3), but at the same time, leads to a sharp drop in ductility and with an increased risk of embrittlement. Based on the phases present, Ti alloys can be classified as α alloys, β alloys or α+β alloys. Within the last category are the subclasses near-α and near-β, referring to alloys with compositions which place them near to α/(α+β) or (α+β)/β-phase boundaries, respectively. The α alloys contain elements such as Al. These α-stabilizing elements increase the phase transformation temperature. They are characterized by satisfactory strength, toughness and weldability but poorer forgeability than β alloys. The absence of ductile-brittle transformation, a property of the (bcc) structure, makes alloys suitable for cryogenic applications. α+β alloys have a composition that supports a mixture of α and β phases. α+β alloys generally exhibit good fabricability as well as high strength in room temperature and moderate elevated-temperature. The most commonly used α+β alloy is Ti-6Al-4V. The β alloys contain elements such as V, Mo, Fe and Cr, which decrease the temperature of the α to β phase transition. β alloys are extremely formable. They are also prone to ductile-brittle transformation, and along

- 6 -

with other bcc-phase alloys, are unsuitable for low-temperature application. The most commonly used Ti alloys are presented in phase-diagram format, to show the interactions between the alloys's α and β-stabilizing components (Fig. 4).

Table 1 Common alloying elements and their stabilizing effect [23]

Alloying element	Range (wt.%)	Effect on structure
Aluminium (Al)	2 to 7	α-stabilizer
Tin (Sn)	2 to 6	α-stabilizer
Vanadium (V)	2 to 20	β-stabilizer
Molybdenum (Mo)	2 to 20	β-stabilizer
Chromium (Cr)	2 to 12	β-stabilizer
Copper (Cu)	2 to 6	β-stabilizer
Zirconium (Zr)	2 to 8	α and β strengthening
Silicon (Si)	0.2 to 1	Improves creep resistance
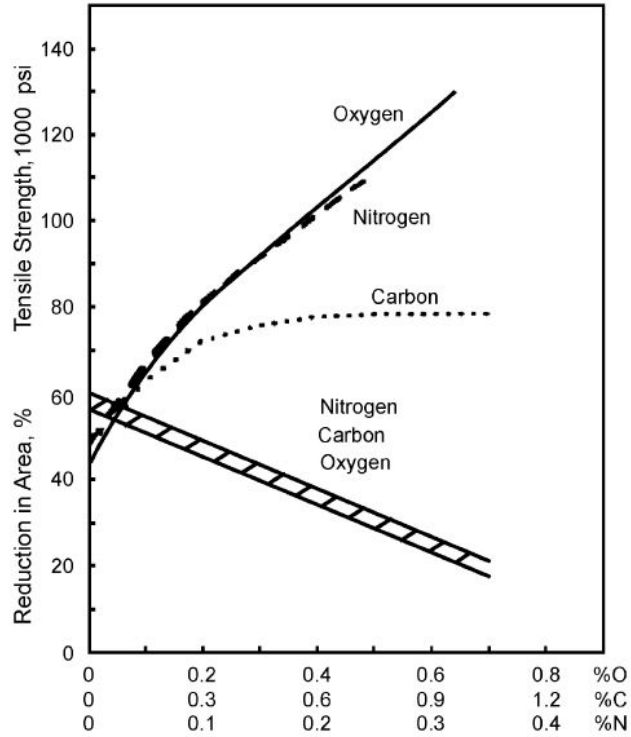
Fig. 3. Effect of interstitial alloying elements on strength and reduction
in area of Ti [24].
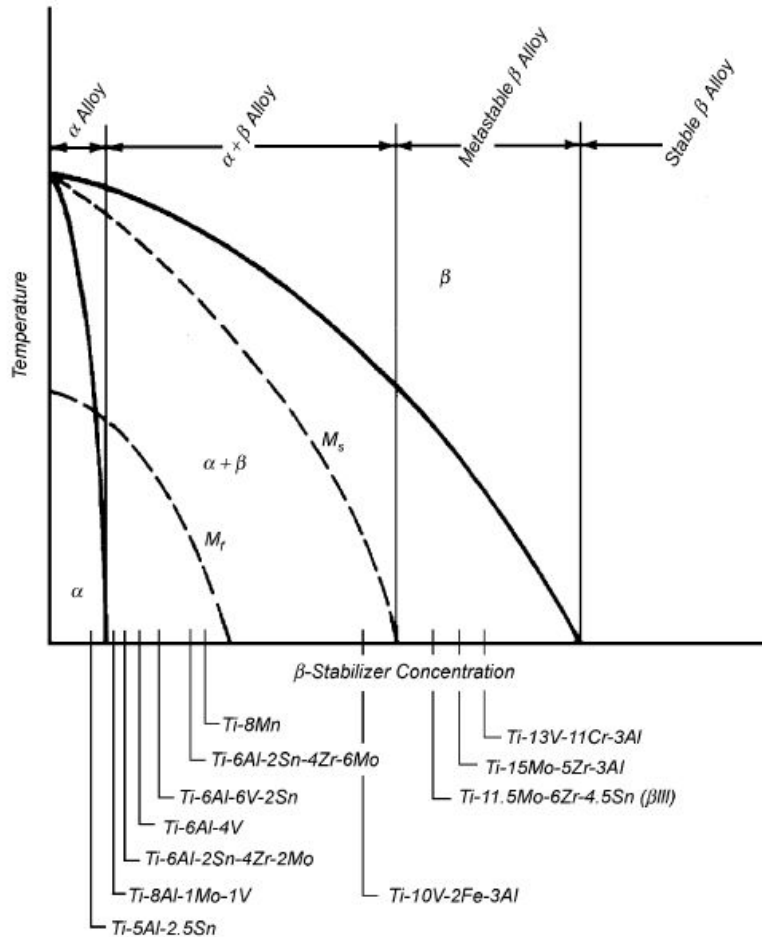
Fig. 4. Compositions of U. S. technical alloys mapped onto a pseudobinary β
-isomorphous phase diagram [25].

2.1.2 Development of Ti alloy for biomedical applications [26]

Recently, Ti alloys are getting much attention for biomaterials because they have excellent specific strength and corrosion resistance, no allergic problems and the best biocompatibility among metallic biomaterials. Pure Ti and Ti-6Al-4V are still the widely used for biomedical applications among the Ti alloys. However, these are basically developed as structural materials mainly for aerospace structures. Therefore, the development of Ti alloys targeted for biomedical applications are highly required. Then the Ti alloys composed of non-toxic elements were started, and are under development with the increasing continuing in common. The Ti non-toxic alloys that have been developed in the early stage are mainly α + β type ones. Recently, biocompatibility is regarded as important factor and therefore the research and development of β types Ti alloys are increasing.

The bioactive surface modifications for improving the biocompatibility of Ti alloys are also increasingly done because the Ti alloys are grouped into bioinert materials by judging from the point of view of patterns of osteogenesis as shown in Table 2.

Furthermore, the direct or indirect evaluation of biocompatibility using animals or cells, and evaluations of mechanical performance such as fatigue, fretting fatigue, fracture toughness, etc. are also energetically done.

Table 2 Biocompatibility of various biomaterials judged by patterns of osteogenesis [26]

Pattern of osteogenesis	Biomaterials	Remarks
Intervened osteoginisis	Stainless steel, Co.Cr alloy, PMMA	Biotolerant materials
Contact osteogenesis	Ti, Ti alloys alloys, carbon, Al, ZrO_2, TiO_2, TiN, Si_3N_4	Bioinert materials
Bonding osteogenesis	Bioglass, ceravital tricalcium phosphate, HA, A.W glass ceramic	Bioactive materials

2.1.3 Ti-Nb alloy system [27]

Ti-Nb alloys demonstrated shape memory alloy (SMA) characteristics at room temperature, and their SMA properties can be considerably improved by thermo mechanical treatment. Because Ti-Nb alloy has metastable β Ti alloy and solution treated it, followed by aging at 482℃. Especially, Ti-35Nb-7Zr-5Ta alloys exhibited 0.2 % off set yield strength of 1,300 MPa with 8 % elongation, due to ω + β and ω + α + β phase precipitation and this enhanced strength makes the alloy as candidate for bone plates and screw [27].

2.2. Nanotube layer on Ti alloy [28]

The successful synthesis of carbon nanotubes by Iijima in 1991 stimulated intense research activities world-wide due to the anticipated technological impact of this unique combination of material, directionality and enhanced properties, such as quantum size effects [28]. In the following years the successful chemical (hydrothermal) synthesis of various other nanotubes, in particular transition metal oxide nanotubes - such as TiO_2 or V_2O_5 was reported. In order to exploit nanotubes in many devices, it is essential to orient nanotubes on substrates and to create ordered arrays. Many different approaches have been explored that mainly are based on lithography, using nano-tools electron-beam, X-ray, ion beam, STM (scanning tunneling microscope), AFM (atomic-force microscopy) or, more elegantly, rely on self alignment processes.

Among the simplest, cheapest and most straight-forward approaches that lead to ordered nanostructures are anodization techniques that can - under the 'right' conditions - lead to highly ordered porous systems (see Fig. 5 (a)). The best explored case is Al and the growth of self-ordered porous alumina layers. For Al, it has been known for decades that porous oxide layers can be grown by anodization typically in acidic electrolytes, while anodization in neutral electrolytes typically leads to a compact oxide layer. However it was not until the remarkable work of Masuda et al [28]. - that it became clear that a very high degree of order can be achieved for these porous geometries. Ordered alumina structures have been proposed, for example, to be used as a photonic crystal structures, or as a template for the deposition of other materials.

More recently, for a range of other metals such as Ti, Zr, Nb, W, Ta and Hf. It has been found that self-organized porous structures can be formed under optimized electrochemical treatments.

2.2.1. Nanotube layer of TiO₂ [29]

TiO₂ nanotube arrays are prepared in a two-electrode aqueous electrolyte system by electrochemical anodization (Fig. 5), in which Ti alloy work as anode and metal Pt as a counter cathode. The formation of TiO₂ nanotube thin films starts with oxidizing the metallic surface, which releases Ti^{4+} ions and electrons (Eq.(1)). An oxide layer is deposited on the metal surface from the chemical interaction of the released Ti^{4+} ions and O^{2-} or OH^- ions of water molecules. Eqs. (2) and (3) describe the formation of hydrated anodic and oxide layer. The TiO₂ is produced from the hydrated anodic layer by a condensation reaction (Eq.(4)). At the cathode Pt surface (Eq.(5)), hydrogen evolution generates and the entire process of oxide formation is expressed in Eq.(6).

$$2Ti \Rightarrow 2Ti^{4+} + 8e^- \qquad (1)$$

$$Ti^{4+} + 4OH^- \Rightarrow Ti(OH)_4 \qquad (2)$$

$$Ti^{4+} + 2O^{2-} \Rightarrow TiO_2 \qquad (3)$$

$$Ti(OH)_4 \Rightarrow TiO_2 + 2H_2O \qquad (4)$$

$$8H^+ + 8e^- \Rightarrow 4H_2 \qquad (5)$$

$$Ti + 2H_2O \Rightarrow TiO_2 + 2H_2 \qquad (6)$$

The F ions in the electrolyte attack the hydrated and oxide layer, where the F^- ions are mobile in the anodic layer and react with Ti^{4+} under the applied electric field. Field-assisted dissolution of the oxide occurs therefore at the interface between oxide and electrolyte. Localized dissolution of the oxide creates small pits (Eqs.(7) and (8)). These locally etched pits act as pore forming centers, which convert into pores uniformly distributed over the whole surface. The pores start to grow at the pore bottom with inward movement of the oxide layer. Ionic species (F^-, O^{2-}, OH^-) migrate from the electrolyte toward the metal/oxide interface. The Ti-O bond undergoes

polarization and is weakened to assist dissolution of the metal cations. Ions Ti^{4+} migrating from the metal to the oxide/electrolyte interface dissolve in the HF electrolyte (Eq.(9)). The free O^{2-} anions migrate toward the metal/oxide interface and further interact with the metal.

$$TiO_2 + 6F^- + 4H^- \Rightarrow TiF_6^{2-} + 2H_2O \qquad (7)$$

$$Ti(OH)_4 + 6F^- \Rightarrow TiF_6^{2-} + 4OH^- \qquad (8)$$

$$Ti^{4+} + 6F^- \Rightarrow TiF_6^{2-} \qquad (9)$$
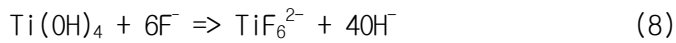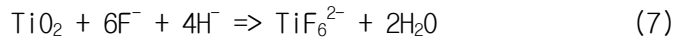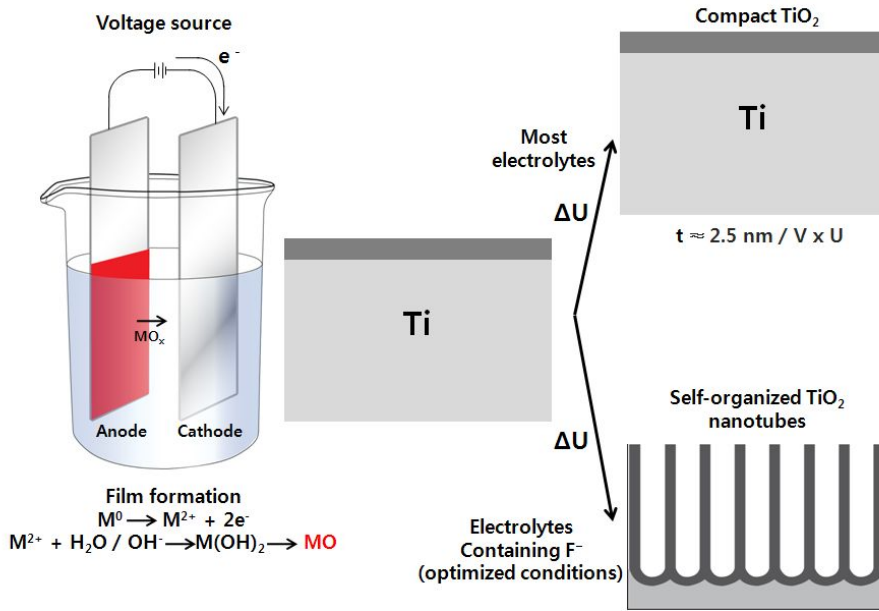
Fig. 5. Schematic set up for anodizing experiments [28, 29].
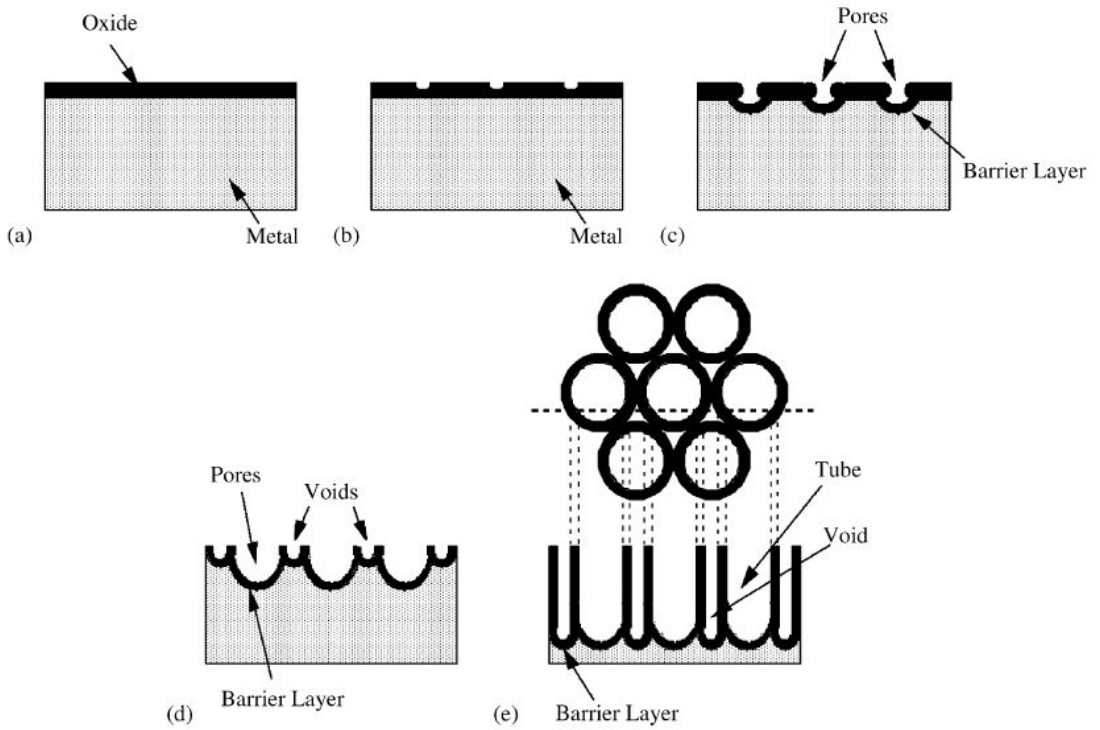
Fig. 6. Schematic diagram of the evolution of a nanotube array at constant anodization voltage: (a) oxide layer formation, (b) pit formation on the oxide layer, (c) growth of the pit into scallop shaped pores, (d) metallic part between the pores undergoes oxidation and field assisted dissolution, and (e) fully developed nanotube array with a corresponding top view [30].

2.3. HA deposited by Electrochemical deposition [31]

Electrochemical deposition are increasingly being used for the preparation of thin films and coatings. The electrochemical deposition has attracted considerable attention recently, because of its low temperature and cost, the control of coating thickness and chemical composition, and the ability to coat irregular implant surface. It is based on an electrode reaction induced pH jump effect. When a current passes through an electrolytic cell, electrons are injected into the solution through cathodic reactions, and drawn out through anodic reactions. The nature of the reactions depends on the electrode potential and the solution conditions. At the cathode, some common reactions are:

$$2H^+ + 2e \rightarrow H_2 \uparrow \text{ (discharge of proton)}$$

$$2H_2O + 2e \rightarrow 2OH^- + H_2 \uparrow \text{ (reduction of molecular water)}$$

$$O_2 \text{ (aq)} + 2H_2O + 4e \rightarrow 4 OH^- \text{ (reduction of dissolved oxygen)}$$
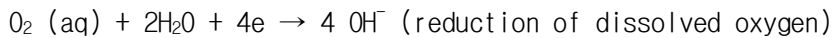
All these reactions can increase the pH of the solution adjacent to the cathode, because of either consuming acid or generating base. In a solution containing Ca^{2+} and phosphate species, the local pH jump drives hydrogen phosphate anions to dissociate and, when the pH reaches a critical point, causes calcium phosphate to crystallize on the cathode to form a coating.

Table 3 Different techniques for HA deposition [32]

Technique	Thickness	Advantage	Disadvantage
Thermal spraying	30~200 μm	High depositon rates; low coast	Line of sight technique; high temperature induce decomposition; rapid cooling produces amorphos coatings
Sputtering coating	0.5~3 μm	Uniform coating thickness on flat substrate; dense coating	Line of sight technique; expansive time consuming; produces amorphous coatings
Pulsed laser deposition	0.05~5 μm	Coating with crystalline and amorphos; coating with dense and porous	Line of sight technique
Dynamic mixing method	0.05~1.3 μm	High adheisve strength	Line of sight technique; expensive; produce amorphous coating
Dip coating	0.05~0.5 mm	Inexpensive; coatings applied quickly; can coat complex substrate	Requires high sintering temperarture; termal expansion mismatch
Sol-gel	< 1 μm	Can coat complex shapes; low processing temperature relatively cheap as coatings are very thin	Some processes require controlled atmosphere processing; expansive raw materials
Electrophoetic deposition	0.1~2.0 mm	Uniform coating thickness; rapid deposition rates; can coat complex substrates	Difficult to produce crack free coating; requires high sintering temp.
Biomimetic coating	< 30 μm	Low processing temp.; can form bonelike apatite; can coat complex shapes; can coat complex shapes; can incorporate bone growth stimulating factors	Time consuming; requires replenishment and a constant of pH of simulated body fluid
Hot isostatic pressing	0.2~2.0 mm	Produce dense coatings	Cannot coat complex substrates; high temp. required; thermal expansion mismatch; elastic property differences; expansive; removal/interaction of encapsulation material

2.4. HA [33, 34]

Biologically relevant CaP belong to the orthophosphate group and naturally occur in several biological structures, including teeth and bone. Bone consists of an inorganic component of biological apatites CaP and an organic component, consisting primarily of collagen and water. Synthetic hydroxyapatite has been demonstrated to have very similar properties to the naturally occurring mineral component of bones and teeth form of calcium apatites. Consequently, CaP have long been investigated and utilized as coatings for protection against wear corrosion and increased biocompatibility in orthopaedic devices. Table 4 summarizes the CaP phases, and a brief review of their properties follows below.

HA theoretically exists as the hydroxyl end-member of apatite, which was suggested in 1912. HA is one of the apatite structures that were observed in rock, the apatite structure has the basic formula $Ca_{10}(PO_4)_6X_2$. X in the formula is the representation group member of apatite and refers to a (OH) group for HA, a F group for fluorapatite, and a (Cl) group for chlorapatite.

HA is a biomaterial with calcium to phosphorus ratio resembles human bone. So, it has been used as a bone replacement material in restorative dental and orthopedic implants. HA can improve bonding strength between body tissues and an implant surface. Also. HA as an implant can bond and promote natural tissue growth.

Table 4 Chemical compositions, Ca/P molar ratio, solubility, pH, and temperature stability range in aqueous solutions of some synthetic and biological calcium orthophosphates [35]

Abb.	Formula	Name	Ca/P ratio	$pk_{sp}(25℃)$	pH stability[a]	Main preparation method	Occurrence in biological tissue
HA	$Ca_{10}(PO_4)_6(OH)_2$	Hydroxyapatite	1.67	116.8	9.5–12	(ⅰ) Titration of $Ca(OH)_2$ with H_3PO_4 (ⅱ) Dropwise addition of HPO_4^{2-} solution to Ca2+ solution, pH>9 (ⅲ) Hydrolysis from other phosphates	Bone, dentin, enamel, dentin calcifications, urinary stones, athorosclerotic plaques
OCP	$Ca_8H_2(PO_4)_6 \cdot 5H_2O$	Octacalcium phosphate	1.33	96.6	5.5–7.0	Dropwise addition of $Ca(Ac)_2$ to $HPO_4^{2-}/H_2PO_4^-$ solutions at 60℃, pH5	Dental and urinary calculi
β-TCP	$Ca_3(PO_4)_2$	β-Tricalcium phosphate (whitlokite)	1.5	28.9	[b]	(ⅰ) Solid state reaction of CaCO3 abd DCPD at 900℃ (ⅱ) Thermal conversion of CDHA	Dental and urinary caculi, soft-tissue deposits, artritic cartilage, usually present as β-TCMP
α-TCP	$Ca_3(PO_4)_2$	α-tricalcium phosphate	1.5	25.5	[b]	Heat treatment of β-TCP at 1300℃	Not found
ACP	$Ca_xH_y(PO_4)_z n H_2O$ n=3~4.5, 15–20%H2O	amorphous calcium phosphate	1.22–2.2	[c]	[b]	Fast mixing of Ca^{2+} HPO_4^{2-} solutions, RT	Soft-tissue calcifications
MCPA	$Ca(H_2PO_4)_2$	monocalcium phosphate anhydrous	0.5	1.14	0–2	Titration of H_3PO_4 with $Ca(OH)_2$ in strong acidic environment	Not found
MCPM	$Ca(H_2PO_4)_2 \cdot H_2O$	monocalcium phospate monohydrate	0.5	1.14	[b]	Heat treatment of MCPM at T>100℃	Not found
DCPD	$CaHPO_4 \cdot 2H_2O$, (brushite)	dicalcium phosphate dihydrate	1.0	6.59	2–6	Dropwise addition of a Ca2+ solution to a HPO42- solution at 60℃, pH4	Dental calculi, urinary stones chondrocalcinosis

Abb.	Formula	Name	Ca/P ratio	pK_{sp}(25℃)	pH stability[a]	Main preparation method	Occurrence in biological tissue
DCPA	$CaHPO_4$, (monetite)	dicalcium phosphate anhydrous	1.0	6.90	[b]	Heat treatment of DCPD at T>100℃	Not found
TTCP	$Ca_4P_2O_9$	tetracalcium phosphate	2.0	38-44	[b]	Solid-state reaction of DCPA with $CaCO_3$ at high T	Not found
CDHA	$Ca_{10-x}(HPO_4)_x(PO_4)_{6-x}(OH)_{2-x}$ (0<x<1)	calcium deficient hydroxyapatite	1.5-1.67	85.1	6.5-9.5	Hydrolysis of ACP or α-TCP	Not found

- 23 -

2.5. Zn substituted HA [36]

HA, with the chemical formula $Ca_{10}(PO_4)_6(OH)_2$, as has been dicussed in previous chapters, belongs to a broad group of calcium phosphates, including tri-calcium phosphate (both α and β) $Ca_3(PO_4)_2O$. In 1926, it was confirmed that the mineral component of bone was in fact a form of HAp. Work by posner and Kay in the 1950s and 1960 using -ray and neutron diffraction determined the structure of HAp [36], It was found that HAp is a hexagonal arrangement of clacium (Ca^{2+}) and phosphate (PO_4^{3-}) ions around monovalent hydroxyl (OH^-) ions. There are wo sites that calcium ions can occupy: site 1-columnar (4 clacium), $c = (0, {}^1/_2, {}^2/_3)$ and $({}^1/_3, {}^2/_3, {}^1/_2)$; and site 2-hexagonal (6 calcium), $c = {}^1/_4$ and ${}^3/_4$. The phosphate groups are located similar to site 2 for the calcium atoms and are in a helical arrangement. The hydroxyl groups are located at the corners of the unit cell in columns parallel to the c-axis.

HA is chemically similar to bone mineral and it lacks the many other ion that are also present in native bone. Substitutions can be made into the HAp lattice to mimic the chemical composition of bone more closely. The first type of substitution is a cationic substitution, where the substituted ions it covers substitutions for both the hydroxyl (type A) and phosphate (type B) groups, A mixed A B type is also possible.

Zn is a cationic substitution; however, until recently, little has been known about the calcium site it substitutes into or indeed the effect of substitution on the HA structure or behavior.
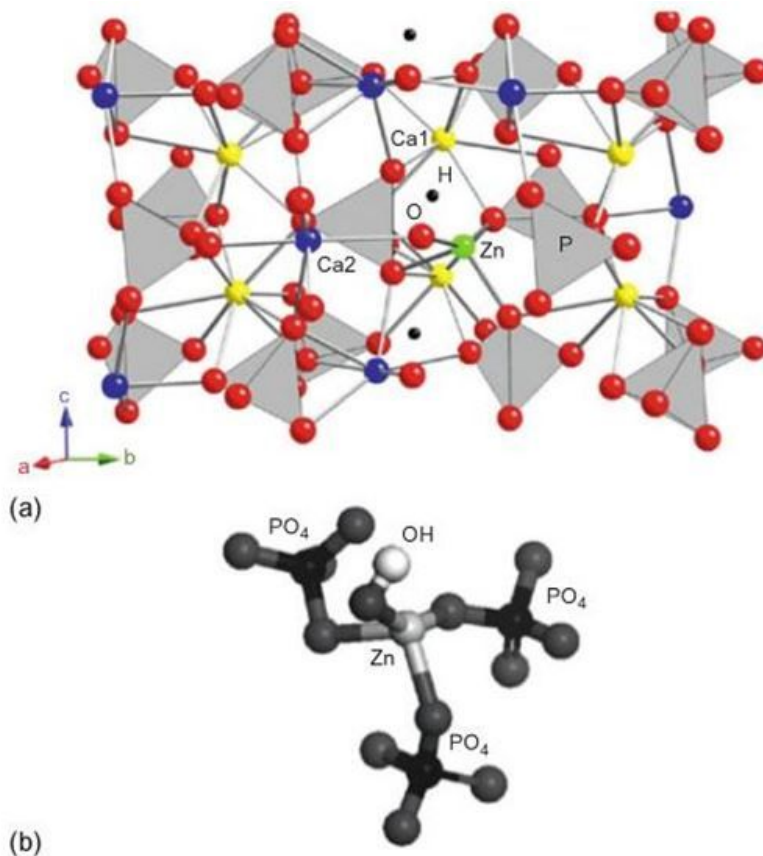
Fig. 7. (a) Optimized structure of Zn-doped HA, Ca^{1}site, Ca^{2}site, O, H, and Zn atoms are shown as yellow, blue, red, black, and green spheres, respectively. Phosphate groups are shown as grey tetrahedra; (b) detailed view of the local coordination of Zn incorporated in HA structure [36].

III. MATERIALS AND METHODS

3.1. Preparation of Ti-xNb alloys

In this research, Ti-xNb binary alloys were Pure Ti (G&S Ti, Grade 4 USA), Nb (Kurt J. Lesker Company, 99.95% purity, USA) contained from 10 to 50 wt.%. Each alloy was melted 10 times to improve chemical homogeneity using a vacuum arc-melting furnace (Model MSTF-1650, MS Eng, Korea). Heat treatment was carried out at 1000℃ for 2 h in a high-purity argon atmosphere and then 0℃ water quenching for homogenization. Heat treated samples were used for various experiments. Also, the specimens were sliced with 2.5 mm thickness and 10 mm diameter by diamond wheel cutter (Accutom-5, Struers, Denmark). The specimens for electrochemical deposition were prepared by using sandpaper grit 100 to 2000 and then given a polish with 0.3 μm Al_2O_3 slurry. All of polished specimens were ultrasonically cleaned in acetone for 10 min and in distilled water and finally dried in air.

3.2. Analysis of surface characteristics for Ti-xNb alloys

The phase and composition of the Ti-xNb alloys surfaces were determined by using an X-ray diffractometer (XRD, X`pert PRO, Philips). Ni-filtered Cu Kα radiation was used in this study. Phase was identified by matching each characteristic peak with JCPDS files. The Ti-xNb alloy surfaces, nanotube surfaces and HA, Zn-HA coated nanotubular surfaces were observed by optical microscopy (OM, Oympus, BX 60M, Japan), field-emission scanning electron microscopy (FE-SEM, Hitachi, S-4800, Japan) and energy dispersive x-ray analysis (EDS, Oxford ISIS 310, England). The etching treatment was performed in Keller's reagent(2 mL HF + 3 mL HCl + 5 mL HNO$_3$ + 190 mL H$_2$O).

3.3. Nanotube formation on the alloy surface

The electrochemical experiments were carried out with a conventional two-electrode configuration consisted of platinum counter electrode and anode working electrode. Before anodization, the sample was embedded with epoxy resin, leaving a square surface area of 10 mm^2 exposed to the anodizing electrolyte. All nanotube formation experiments were carried out at constant voltage (30 V) for 1 h (D.C) power source (Model E3641A, Agilent Technologies, Palo Alto, USA). The electrolyte was composed of 1 M H_3PO_4 containing 0.8 wt.% NaF. The morphology of the porous Ti oxide was characterized by a FE-SEM.

3.4. HA and Zn-HA deposited on nanotubular Ti-xNb alloys

Electrochemical deposition of pure HA and Zn doped HA were conducted at 85 ℃ in an electrolyte containing (HA) 5 mM $Ca(NO_3)_2 \cdot 4H_2O$ + 3 mM $NH_4H_2PO_4$ and 4.95 mM $Ca(NO_3)_2 \cdot 4H_2O$ + 0.05 mM $Zn(NO_3)_2 \cdot 4H_2O$ + 3 mM $NH_4H_2PO_4$ in distilled water (Zn-HA); the Ca/P ratio for the electrolyte was 1.67 ratio. Electrolytes were not including the component of the Mg^{2+}, K^+, Cl^- and CO^{3-}, in order to avoid carbonate generation and contamination during HA and Zn doped HA deposition process. Precipitation of pure HA and Zn doped HA was performed on the bulk Ti-xNb alloy surfaces using a potentiostat (PARSTAT2273, Princeton Applied Research, USA). The deposition was carried out by cyclic voltammetry (CV) the potential between -1500 mV to 0 V at scan-rate 100 mV/s, followed by a break time (tb) of 2 s. The number of cycle employed for this electrochemical Zn-HA deposition, performed at 85℃, was 30 cycle. The pulsing cycle was schematically illuatrated in Fig. 8. Also, the electrodeposition condition of Zn-HA deposited surface are summarized in Table 5.

The surface morphology and chemical composition were observed with a FE-SEM, EDS and mapping analysis. The crystal phase of the deposit was examined using a thin film X-ray diffractometer (TF-XRD, X'Pert Pro, and Philips, Netherlands). TF-XRD analysis was done using a XRD with Cu Kα incident radiation.
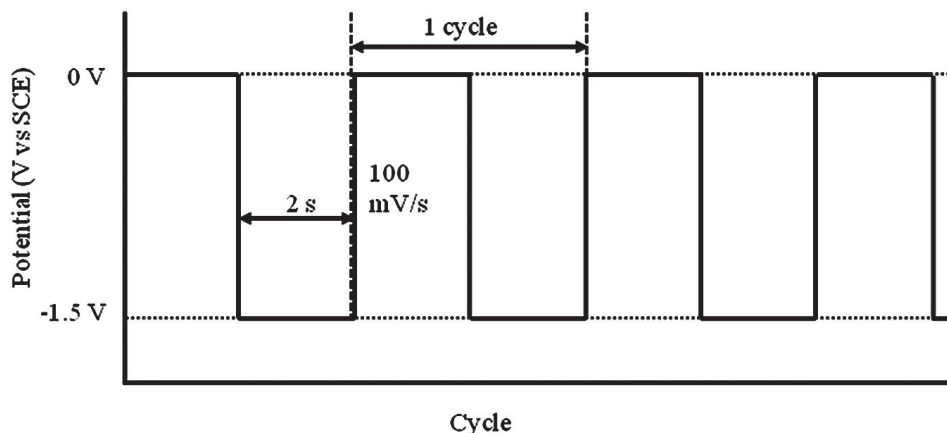
Fig. 8. Process of monitoring voltage versus cycles during the formation of
Zn-HA deposition [37].

Table 5 Electrochemical deposition condition of HA and Zn-HA deposition

Coating condition	
Equipment	Cyclic voltammetry (CV)
Reference electrode	saturated calomel electrode
Counter electrode	Pt
Electrolyte	(HA) 5 mM $Ca(NO_3)_2 \cdot 4H_2O$+ 3 mM $NH_4H_2PO_4$
	(Zn-HA) 4.95 mM $Ca(NO_3)_2 \cdot 4H_2O$ + 0.05 mM $Zn(NO_3)_2 \cdot 4H_2O$ + 3 mM $NH_4H_2PO_4$
Working temp.	85 ± 1℃
Scan rate	100 mV/s
Cycle number	30

Ⅳ. RESULTS AND DISCUSSION

4.1. Microstructures of Ti-xNb alloys

Fig. 9 and Fig. 10 show the OM and FE-SEM analysis results for the microstructures of the Ti-xNb alloys with Nb content 10, 30 and 50 wt.% after heat treatment at 1000℃ for 2 h in Ar atmosphere, followed by 0℃ water quenching. Fig. 9 (a), (b) and (c) show results of OM images and, Fig. 10 (a), (b) and (c) show results of FE-SEM images. The Ti-10Nb and Ti-30Nb binary alloys had needle-like and martensitic structure with α and α″ phase (Fig. 9 (a), (b) and Fig. 10 (a), (b)). It was corresponded with previous research [27] results; the Ti-xNb alloys with Nb present in 17.5 ~ 25 wt.% Nb were the primarily comprised an orthorhombic α″ phase. However the Ti-50Nb alloy have less needle-like trace than Ti-10Nb alloy surface and showed equiaxed structure with β phase (Fig. 9 (c) and Fig. 10 (c)). Thus, Fig. 9 and Fig. 10 show that the apparent volume fraction of martensite decreased with increasing Nb content in the Ti-xNb alloys. This may be associated with the enhancement of β-phase stability with increasing Nb content, since Nb is a known β-phase stabilizer [38, 39].

Fig. 11 shows the XRD patterns of Ti-xNb alloys. All kind of peaks were identified using the JCPDS diffraction data for element standards. Fig. 11 XRD patterns of (a) Ti-10Nb, (b) Ti-30Nb, and (C) Ti-50Nb alloy, respectively. Ti-10Nb alloy showed the peaks of (100), (002), (101), (102), (103), and (112) from α phase structure, whereas Ti-30Nb alloy showed the peaks of (110), (021), and (103) from orthorhombic α″-phase and β-phase. Also, Ti-50Nb alloy showed (110), (021), (200), and (211) from only β-phase [40] as shown in Fig. 11. When the Nb content increased to 50 wt.%, the alloy was comprised entirely of equiaxed β phase grains. As a result α and α″ phase occurs with Nb contents and the β phase is found when Ti is alloyed with the larger Nb content. It is consistent to the microstructures

on the Ti-50Nb alloy by Fig. 9 (c) and Fig. 10 (c) images. Besides, it is considered that the addition of Nb element to Ti alloy plays role to inhibit the formation of the metastable α″ martensitic phase and transformed the β phase during quenched heat treatment [41].
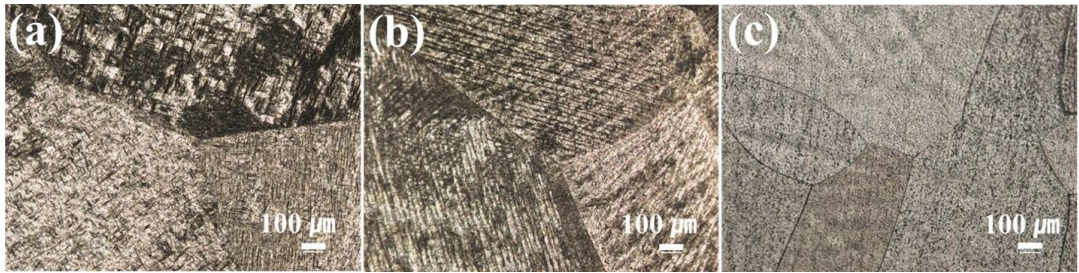
Fig. 9. OM images of Ti-xNb alloys after heat treatment at 1000℃ for 2 h in Ar atmosphere, followed by 0℃ water quenching: (a) Ti-10Nb, (b) Ti-30Nb, (c) Ti-50Nb.
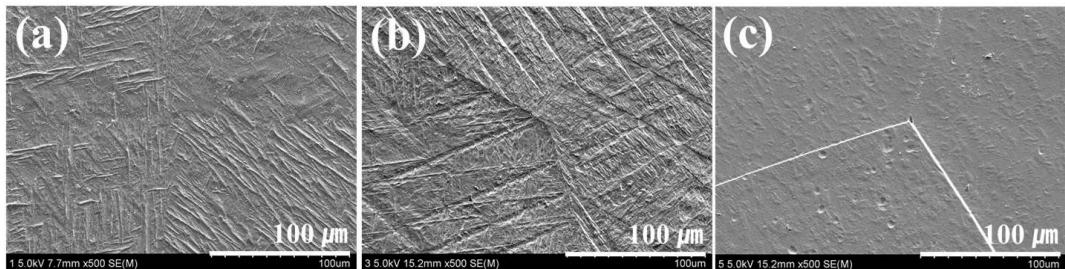
Fig. 10. FE-SEM images of Ti-xNb alloys after heat treatment at 1000℃ for 2 h in Ar atmosphere, followed by 0℃ water quenching: (a) Ti-10Nb, (b) Ti-30Nb, (c) Ti-50Nb.
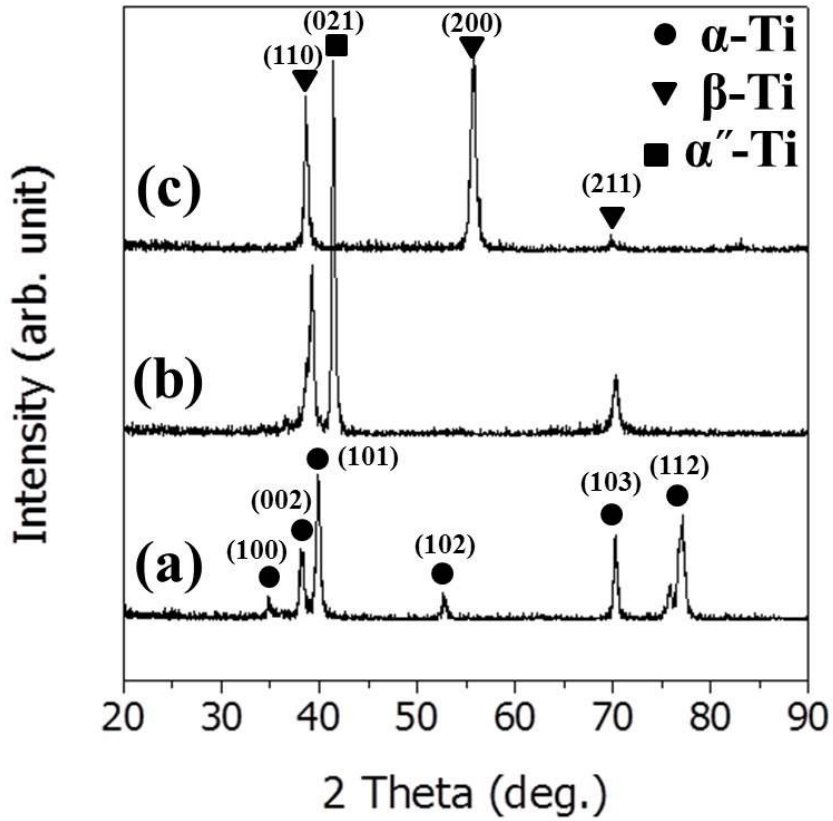
Fig. 11. XRD patterns of Ti-xNb alloys after heat treatment at 1000℃ for 2 h in Ar atmosphere, followed by 0℃ water quenching: (a) Ti-10Nb, (b) Ti-30Nb, (c) Ti-50Nb.

4.2. The HA deposited on the Ti-xNb alloys by electrochemical deposition

Fig. 12 shows FE-SEM images of the HA films deposited on the Ti-xNb alloys after 30 electrochemical cycles in the first electrolyte (CaP solution). The surfaces of these Ti-xNb alloy specimens were partially covered with a nano-scale rod-like HA layer, as shown in Fig. 12 (a-c). As the Nb concentration increased, high-density nano-scale needle-like precipitates formed, as shown for the Ti-50Nb alloy. It is evident that the amount of Nb in the binary Ti alloys strongly influences the HA nucleation and growth processes. The cross-sections in these images were acquired from mechanically scratched samples where some pieces flaked off and were upside down. The average width of the HA layer appeared 0.41, 0.45, and 0.44 µm for the Ti-10Nb, Ti-30Nb, and Ti-50Nb alloys, respectively it is conjectured that the morphology of these surface precipitates depends mainly on substrate morphology. For the bulk surface of the Ti-50Nb alloy, HA nuclei formed at β phase sites, grew rapidly, and Ti-xNb alloys surface, eventually assuming the rod-like morphology. As shown in Fig. 12 (a-1, b-1, and c-1), the FE-SEM results show that all of the surface regions containing HA layers were composed of Ca, P and the Ti-xNb alloys, with overall compositions in good agreement with the nominal compositions of HA and the binary Ti alloys. The Ca/P ratios of the HA coating layers calculated from the EDS analyses are indicated in table 6, namely 1.49, 1.57, and 1.62, respectively. These results were lower than the Ca/P ratio of 1.67, which corresponds to the standard stoichiometry for HA.
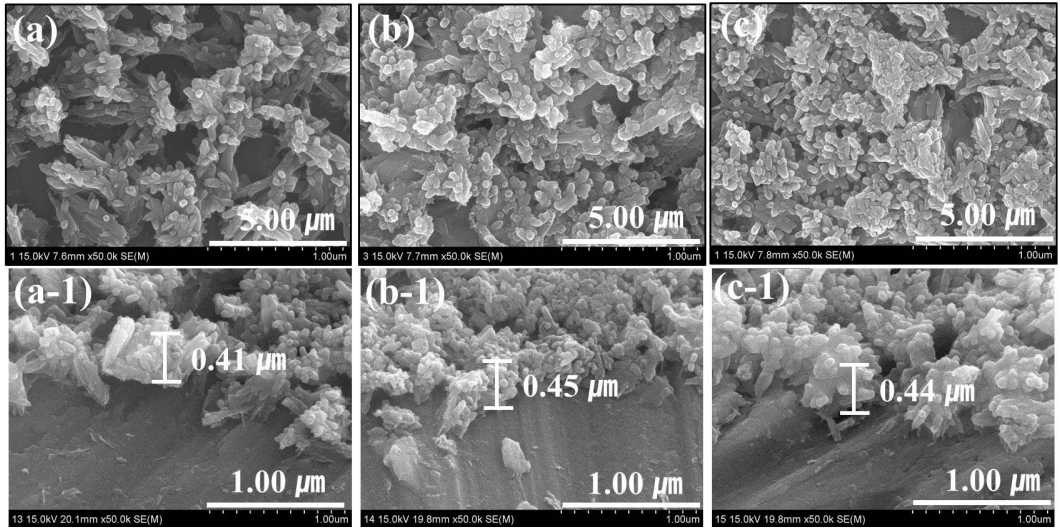
Fig. 12. FE-SEM images of HA deposited on the Ti-xNb alloys: (a), (a-1) Ti-10Nb; (b), (b-1) Ti-30Nb; (c), (c-1) Ti-50Nb.

4.3. The Zn-HA deposited on the Ti-xNb alloys by electrochemical deposition

Fig. 13 shows FE-SEM images of the Zn-HA layers deposited on the Ti-xNb alloys, formed after 30 electrochemical cycles in the second electrolyte (Zn-HA). Fig. 13 (a-c) shows that nano-scale network-like layers were created on the Ti-xNb alloys. As the Nb content increased, the Zn-HA layers assumed an increasing nano-scale network character and denser morphology. The coating thicknesses were determined to 0.53, 0.51, and 0.55 μm, respectively, for increasing 10, 30 and 50 wt.% of Nb. EDS analyses, shown in Table 6, revealed the presence of Ca, Zn, P, O, Ti, and Nb in the near-surface regions of the Zn-HA layers. Calculations indicated that the Zn-HA layers on the Ti-10Nb, Ti-30Nb and Ti-50Nb alloys contained approximately 1.51, 1.35, and 1.48 wt.% Zn, respectively.
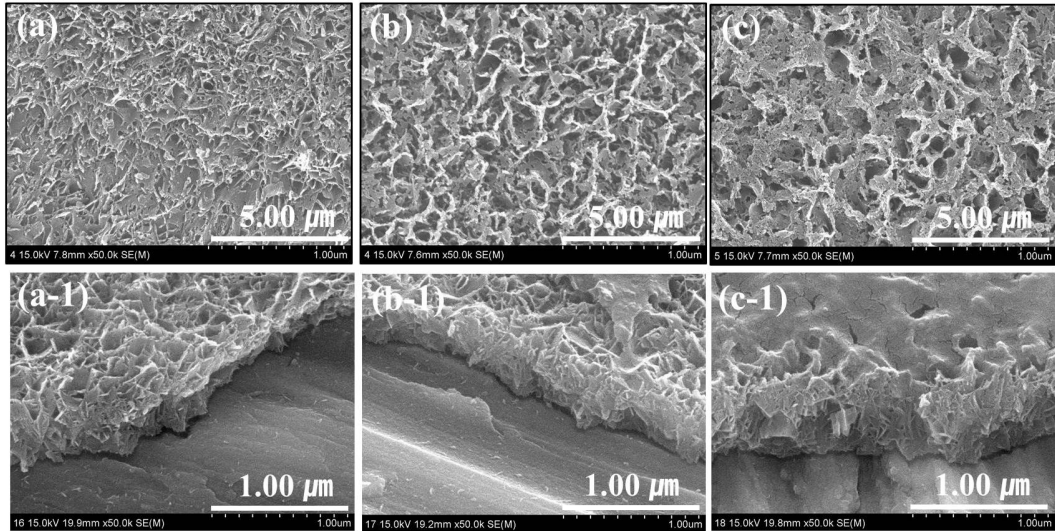
Fig. 13. FE-SEM images of Zn-HA deposited on the Ti-xNb alloys: (a), (a-1) Ti-10Nb; (b), (b-1) Ti-30Nb; (c), (c-1) Ti-50Nb.

Table 6 EDS analysis results of HA and Zn-HA deposited on the Ti-xNb alloys

Specimens	Elements						
	Ti	Nb	Ca	P	Zn	O	Totals
Ti-10Nb (HA)	56.04	7.61	3.22	2.15	0.00	30.98	100.00
Ti-30Nb (HA)	45.53	21,56	3.05	1.94	0.00	27.92	100.00
Ti-50Nb (HA)	33.02	37.66	2.52	1.56	0.00	25.24	100.00
Ti-10Nb (Zn-HA)	40.14	4.97	8.20	5.86	1.51	39.32	100.00
Ti-30Nb (Zn-HA)	30.64	14.86	8.03	5.39	1.35	39.73	100.00
Ti-50Nb (Zn-HA)	21.80	25.42	8.16	5.29	1.48	37.85	100.00

4.4. The TF-XRD patterns results of Zn-HA deposited on the Ti-xNb alloys by electrochemical deposition

Fig. 14 shows TF-XRD patterns of the HA and Zn-HA layers on the Ti-xNb alloys formed after 30 electrochemical deposition cycles in the HA and Zn-HA electrolytes. XRD peaks corresponding to HA were observed for all samples, closely matching those in JCPDS file for the HA powder standard. Furthermore, the HA (002) diffraction peak was observed for deposits formed in both the HA and Zn-HA electrolytes, indicating c-axis orientation of the HA crystals. Fig. 14 (c) shows that the position of HA (002) peak was shifted slightly to a higher angle for Zn-HA (2θ = 25.89 deg) compared to HA (2θ = 25.86 deg). Therefore, this lattice parameter of Zn-HA decreased as Zn^{2+} ions replaced Ca^{2+} ions in the HA lattice. This result was consistent with the smaller ionic radius of Zn^{2+} compared with Ca^{2+} (0.075 nm and 0.099 nm, respectively). The peaks in Fig. 14 (b) were also identified as HA (now designated as Zn-HA); in the case of Zn-HA deposition, the XRD peaks of the samples became broader compared to Fig. 14 (a), indicating lower crystallinity due to addition of Zn^{2+} ions to the HA crystal structure. When the Zn concentration increased in the electrochemical deposition solution, the crystalline apatite structure was no longer sustained, and the precipitated coating became amorphous. At higher Zn concentrations, the precipitates were found in the study by another group to become different calcium Zn phosphates.
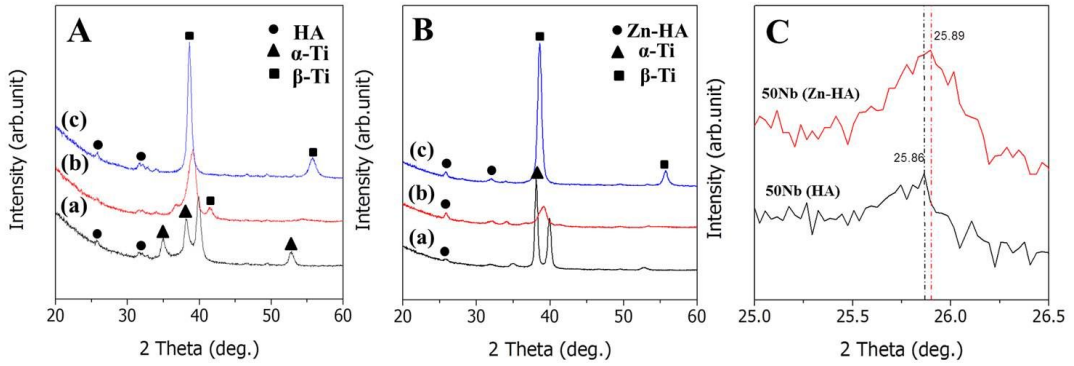
Fig. 14. TF-XRD patterns of HA and Zn-HA deposited on the Ti-xNb alloys:
(a), (a-1) Ti-10Nb; (b), (b-1) Ti-30Nb; (c), (c-1) Ti-50Nb.

4.5. The nanotube surface of Ti-xNb alloys

Fig. 15 shows the FE-SEM images and EDS analysis of the nanotube formed on the Ti-xNb alloys surface. The nanotubular structure of Ti-10Nb shows an irregular distribution, whereas nanotubes of the Ti-30Nb and Ti-50Nb alloys were highly ordered distribution consisted of two distinct diameters; large tubes are surrounded by several smaller tubes. In Fig. 15 (a) of Ti-10Nb alloys, it can be estimated that the nanotubes have the 150 nm. However, in Fig. 15 (b) of Ti-30Nb alloy, nanotube diameter is the 120 nm and Ti-50Nb alloy (c) has the 100 nm. It is well known that reduction of nanotube diameter with Nb content is because of formation of Nb oxide on the surface [41, 42]. Also, these researchers reported that the changes of alloy composition, applied voltage, anodization time, and electrolytic composition can change the dimensions of the nanotube. Fig. 15 (a-1), (b-1), and (c-1) show the EDS peaks of elements with overall compositions consistent with the nominal composition of the Ti-xNb system. The Nb content increased in order of 10, 30, and 50 wt.%. It is confirmed that the alloy compositions play role the formation of the various nanotube morphology in the oxide layer during reaction of fluoride ion and metallic ions in the oxides like Nb_2O_5 and TiO_2 [43].

Table 7 shows the EDS analysis results of non-nanotube formed Ti-xNb alloys and nanotube formed Ti-xNb alloys at 30 voltage. In the Ti-10Nb, Ti-30Nb, and Ti-50Nb alloys, the composition of the alloy was well consistent with designed alloys.

Fig. 16 shows XRD patterns from nanotubular surface of the Ti-xNb alloys with Nb contents. Fig. 16 (a), (b), and (c) are XRD patterns of nanotube formed Ti-10Nb, Ti-30Nb, and Ti-50Nb alloy, respectively. Ti-10Nb alloy showed the peaks of (100), (002), (010), (102), (103), and (112), whereas Ti-30Nb alloy showed the peaks of (100), (002), (200), and (211). Also, Ti-50Nb alloy showed (110), (200), and (211). The peaks showed mainly α-Ti and β-Ti. The crystallinity of the nanotubes has relevance for the

- 42 -

biocompatibility and corrosion resistance of the Ti alloy. But, in Fig. 16, comparing to XRD patterns of non-treated Ti-xNb alloy of Fig. 11, the XRD pattern shows the lower and broader intensity. It means that amorphous phases are formed on the surface. The XRD peaks of crystallized TiO_2 can observe at 2θ=25.5° and 27.58° for anatase and rutile phase [44]. If the amorphous Ti oxides are heated at 500℃ for 2 h in air atmosphere, Ti oxides can be converted to the crystalline TiO_2 anatase and rutile phases [43]. In Fig. 16, peaks of non-heat treated alloys showed the irregularity line and a little sharpness compared to Fig. 11. Therefore, it is thought that nanotube surface consisted of some amorphous and some crystalline structures. Generally, it was reported that anatase structures had a good biocompatibility due adoptable structures to cell [44].
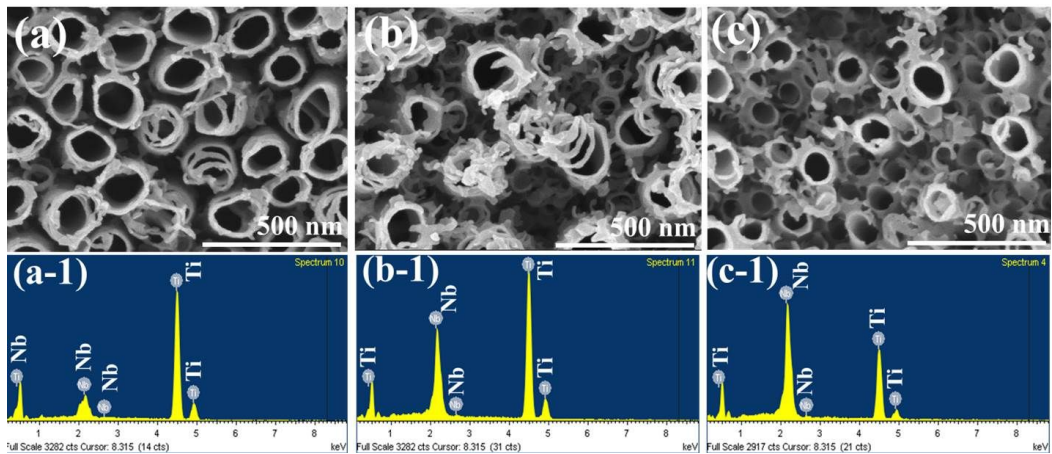
Fig. 15. FE-SEM images and EDS analysis result of TiO₂ nanotubes formed on Ti-xNb alloys: (a), (a-1) Ti-10Nb; (b), (b-1) Ti-30Nb; (c), (c-1) Ti-50Nb.

Table 7 EDS analysis results of non-nanotube formed Ti-xNb alloys and nanotube formed Ti-xNb alloys at 30 voltage

Specimens	Elements		
	Ti	Nb	Total
Ti-10Nb	88.48	11.52	100.00
Ti-30Nb	67.70	32.30	100.00
Ti-50Nb	44.07	55.93	100.00
Ti-10Nb Nanotube	92.62	7.38	100.00
Ti-30Nb Nanotube	69.82	30.18	100.00
Ti-50Nb Nanotube	45.79	54.21	100.00
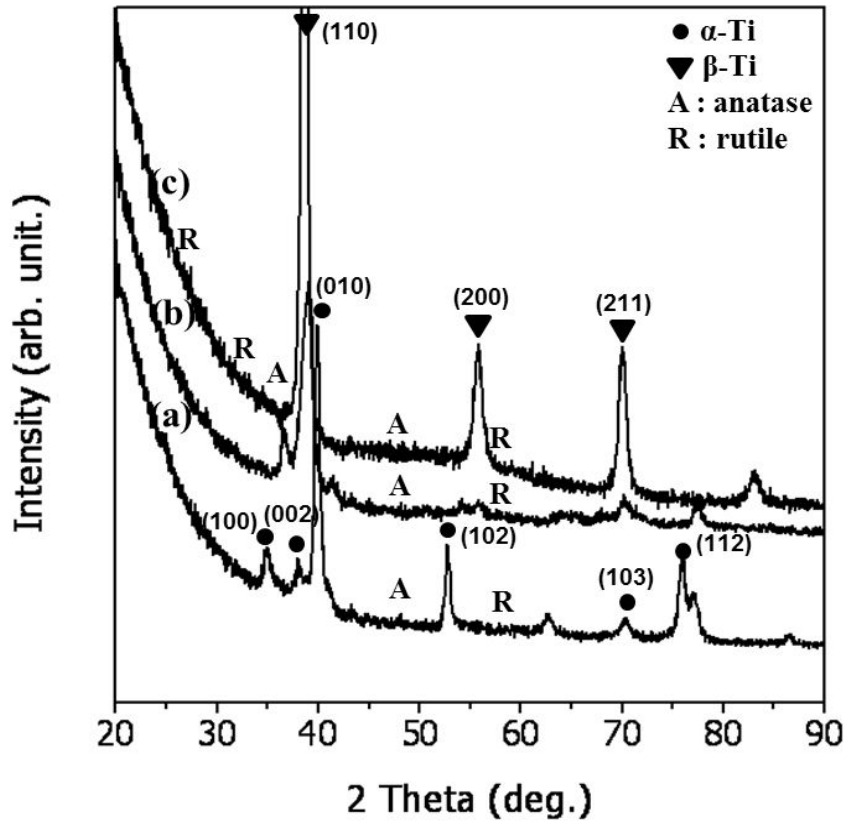
Fig. 16. XRD patterns of TiO₂ nanotubes formed on Ti-xNb alloys: (a) Ti-10Nb, (b) Ti-30Nb, (c) Ti-50Nb.

4.6. The HA and Zn-HA deposited after nanotube formation on the Ti-xNb alloys by electrochemical deposition

Fig. 17 shows FE-SEM images of the HA and Zn-HA deposited on the Ti-xNb alloys for 30 cycles by electrochemical deposition after the nanotube formation. Fig. 17 (a) and (a-1), the top of nanotube was covered with HA and Zn-HA precipitated with the increasingly larger plate of HA and smaller particles surrounding pores that lose the nanotube pore. And in Fig. 17 (b), (c) and (b-1), (c-1), the precipitate particle sizes of HA and Zn-HA decreased with Nb content due to different nanotube size as above mentioned on nanotube formation, and in the case of Zn-HA coated surface, all the surface was covered with small particle deposits. It is confirmed that Zn ions act as competitor and inhibitor against Ca for nucleation of HA. In Fig. 17 (c) and (c-1), images of HA and Zn-HA deposited on Ti-50Nb alloy after the nanotube formation is very similar in morphology. However, Fig. 17 (a) and (a-1) is different from each other on the surface. Fig. 17 (a) showed the flower-like and larger size of nanotube surface could not entirely be covered with particle. If the nuclei of HA precipitate on the top of large size tube, nuclei can be easily grown and spread without interference by like a Zn ion. However in Fig. 17 (a-1), the Zn-HA deposited surface after nanotube formation was covered with small particles on almost the nanotube surface. It is assumed that Zn ion can act as nuclei in the process of deposition and can substitute to Ca in the HA structure.

Fig. 17. FE-SEM top images the HA and Zn-HA deposited on the nanotube formed Ti-xNb alloys for 30 cycles by electrochemical deposition. (a) HA deposited Ti-10Nb alloy; (b) HA deposited Ti-30Nb alloy; (c) HA deposited Ti-50Nb alloy; (a-1) Zn-HA deposited Ti-10Nb alloy; (b-1) Zn-HA deposited Ti-30Nb alloy; (c-1) Zn-HA deposited Ti-50Nb alloy.

4.7. The cross-section views of HA and Zn-HA deposited after nanotube formation on the Ti-xNb alloys by electrochemical deposition

Fig. 18 shows FE-SEM images of cross-section views of the HA and Zn-HA deposited after nanotube formation on the Ti-xNb alloys for 30 cycles by electrochemical deposition. In Fig. 18 (a-1) and (a), there was no difference in the two images, but the cross-section image and the length of HA and Zn-HA deposited after nanotube formation increased as the Nb content increased. As shown in Fig. 18 (a-1) to (c-1), layer of Zn-HA from the cross-section FE-SEM images shows that as the average length of the nanotube formed HA and Zn-HA films generally increased as Nb content increased from 10 to 50 wt.%; cross-sectioned nanotube layer of Ti-10Nb alloy is averages 110 nm, Ti-30Nb 227 nm, Ti-50Nb is 230 nm thicknesses, respectively. Also the layers Zn-HA and HA was deposited on the nanotube.
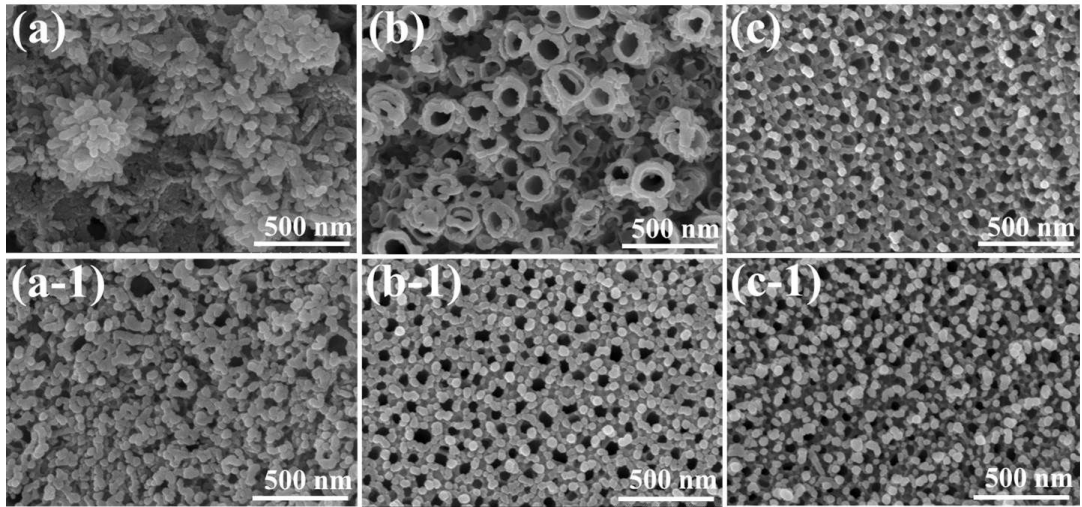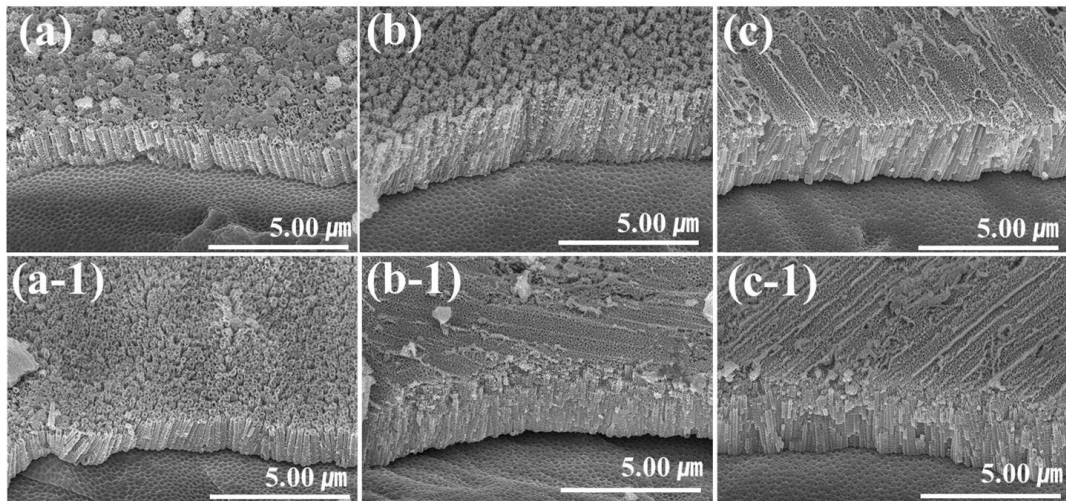
Fig. 18. FE-SEM cross-section images of the HA and Zn-HA deposited on the nanotube formed Ti-xNb alloys for 30 cycles by electrochemical deposition. (a) HA deposited Ti-10Nb alloy; (b) HA deposited Ti-30Nb alloy; (c) HA deposited Ti-50Nb alloy; (a-1) Zn-HA deposited Ti-10Nb alloy; (b-1) Zn-HA deposited Ti-30Nb alloy; (c-1) Zn-HA deposited Ti-50Nb alloy.

4.8. The surface morphology and structures of HA and Zn-HA deposited after nanotube formation on the Ti-xNb alloys

Fig. 19 shows the TF-XRD patterns of (A) HA and (B) Zn-HA deposited on the (a) Ti-10Nb, (b) Ti-30Nb, and (c) Ti-50Nb alloys for 30 cycles by electrochemical deposition after nanotube formation. The TF-XRD patterns of HA and Zn-HA were observed in the coated surface. The peaks were clearly indicative of HA and Zn-HA shown throughout the pattern with 2-theta values that correspond closely to those observed in the JCPDS file for (A) HA and (B) Zn-HA. In Fig. 19 (A), the peaks of HA deposited on the Ti-xNb alloys after nanotube formation were smaller than those of matrix (nanotube formed surface). It means that coated layer is very thin compared to nanotubular layer. In this figure, main peak is alloy from matrix, (110) peak is higher than those of others as Nb content increases as shown in Fig. 11, it was confirmed the β-phase. Additionally, HA peak was confirmed the position of (002). Fig. 19 (B) shows peaks of Zn-HA deposited on the (a) Ti-10Nb, (b) Ti-30Nb, and (c) Ti-50Nb alloys after nanotube formation. When the Zn-HA was deposited in Fig. 19, Zn-HA peaks were smaller than those of anatase, rutile, and matrix. As Zn concentration increases in the electrochemical deposition solution as shown in Table 8, a crystalline apatite structure (HA) is no longer remained, and change to an amorphous structure [44]. At high Zn concentration, other calcium precipitates, the other group will be a Zn phosphate found in the deposited surface. Therefore, XRD peaks of Zn-HA deposition surface showed broaden and lower than those of matrix. Table 8 shows the EDS analysis results of HA and Zn-HA deposited on the Ti-xNb alloys after nanotube formation. From the EDS results, HA deposited Ti-xNb alloys showed O, Ca, and P elements and contents were detected. Also, Zn, Ca, and P were detected according to the HA (Ca/P) content conditions.
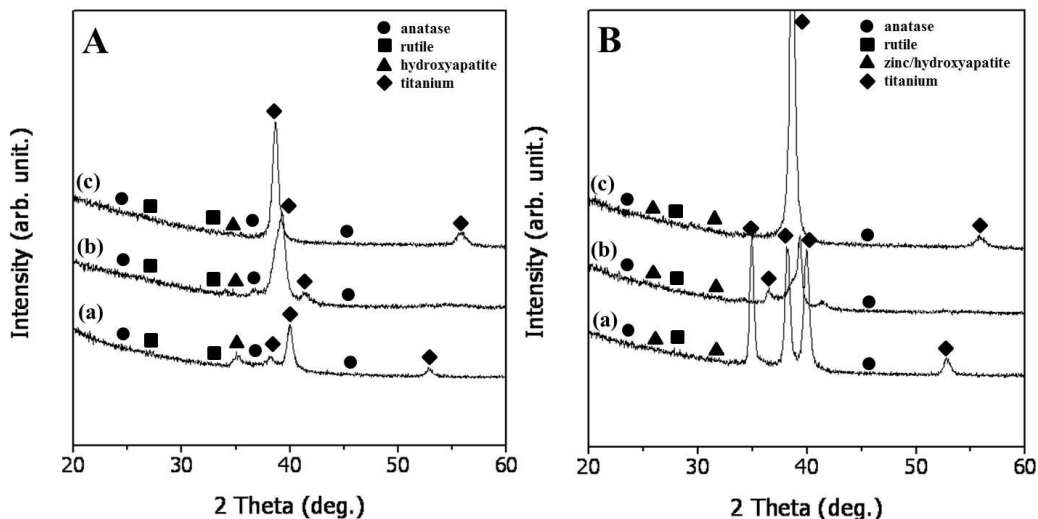
Fig. 19. TF-XRD patterns of the nanotube formed (A) HA and (B) Zn-HA deposited on the (a) Ti-10Nb alloy, (b) Ti-30Nb alloy, (c) Ti-50Nb alloy for 30 cycles by electrochemical deposition.

Table 8 EDS analyses result of nanotube formed HA and Zn-HA deposited on the Ti-xNb alloys

Specimens	Elements						
	Ti	Nb	Ca	P	Zn	O	Totals
Ti-10Nb (HA)	56.44	1.28	4.00	3.64	0.00	34.64	100.00
Ti-30Nb (HA)	42.92	15.56	0.42	1.59	0.00	39.52	100.00
Ti-50Nb (HA)	33.37	34.64	0.30	1.55	0.00	30.14	100.00
Ti-10Nb (Zn-HA)	61.46	0.08	0.14	1.28	0.50	36.54	100.00
Ti-30Nb (Zn-HA)	45.42	15.98	0.45	1.58	1.56	35.00	100.00
Ti-50Nb (Zn-HA)	38.81	42.52	0.34	1.72	0.27	16.25	10.00

Fig. 20 shows the EDS mapping results of HA deposited on the Ti-10Nb and Ti-50Nb alloys. Fig. 20 (a) is HA deposited Ti-10Nb image, (b) is EDS mapping image of Ca and P, (c) is HA deposited Ti-50Nb image, and (d) is EDS mapping image of Ca and P. In Fig. 20 (b), Ca and P were distributed ununiformly in the flower like precipitates in the case of larger nanotube size of Ti-10Nb which was partially covered with precipitates, whereas Ca and P were uniformly distributed on the deposited Ti-50Nb alloy whole covered with deposites on the small sized nanotube as shown in Fig. 17.

Fig. 21 shows the EDS mapping results of Zn-HA deposited on the Ti-10Nb and Ti-50Nb alloys. In the case of Zn-HA coating surface, whole surface area showed the uniform distribution of coated elements on the nanotubular surface. Also, in the case of small nanotube size of Ti-50Nb alloy, element distribution showed more and more uniform on the whole surface. Therefore, It is confirmed that Zn can play role to nucleate the Zn-HA on the top of nanotube and interspace between tube and tube.

Fig. 20. EDS mapping result of nanotube formed HA deposited on the Ti-xNb
alloys: (a) FE-SEM images of Ti-10Nb alloy; (b) mapping images of
Ti-10Nb alloy; (c) FE-SEM images of Ti-50Nb alloy; (d) mapping
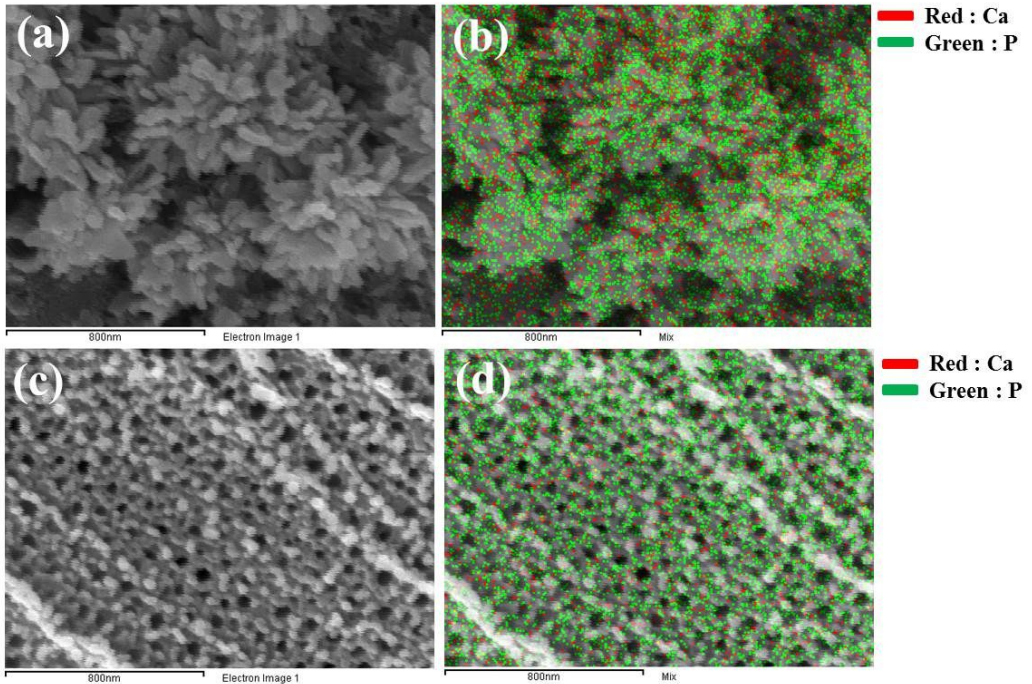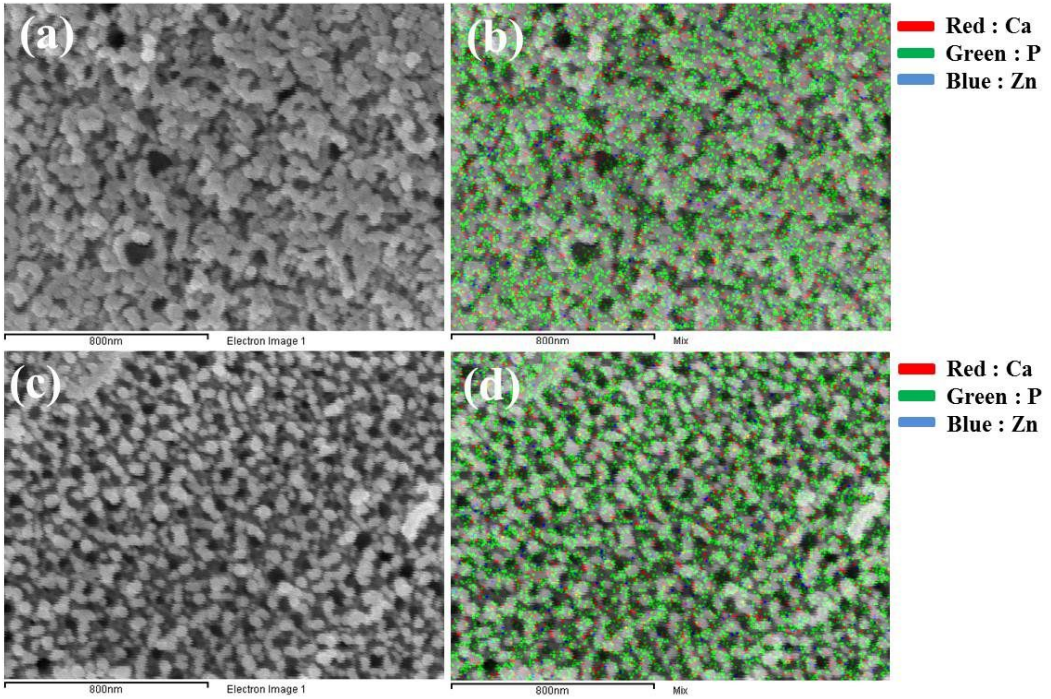images of Ti-50Nb alloy.

Fig. 21. EDS mapping result of nanotube formed Zn-HA deposited on the Ti-xNb
        alloys: (a) FE-SEM images of Ti-10Nb alloy; (b) mapping images of
        Ti-10N alloy; (c) FE-SEM images of Ti-50Nb alloy; (d) mapping images
        of Ti-50Nb alloy.

Ⅴ. CONCLUSIONS

In this study, we investigated surface characteristics of HA and Zn-HA coatings on the nanotubular Ti-xNb alloys by electrochemical deposition method.

The results were as follows;

1. Microstructures of the alloys were transformed form α'' phase to β phase, Ti-10Nb alloy exhibits was mainly composed of needle-like structure assumed to α and β phase. Ti-30Nb exhibited alloy showed the needle-like and equiaxed structure assumed to martensitic α'' phase. In the case of Ti-50Nb alloy, most of microstructure showed equiaxed structure.

2. The nanotubular structure of Ti-10Nb, Ti-30Nb, and Ti-50Nb alloys showed the irregular structure. As Nb content increased, nanotube length of Ti-xNb alloys increased.

3. In the case of HA coated surface, nano rod-like shape of precipitate showed and nano network-like shape in the case of Zn/HA coated surface.

4. The top of nanotube was covered with HA and Zn-HA precipitated with the increasingly larger plate of HA and smaller particles surrounding pores.

5. In the case of HA deposited on the nanotubular Ti-xNb alloys, Ca and P were uniformly distributed on the coated layer. In the case of Zn-HA deposited surface, Ca, P, and Zn were well distributed on the surface.

In conclusion, unifrom Zn-HA coated Ti-xNb alloy can be applicated to improve the osseointegration in the bone.

- Reference -

1. T.I. Kim, J.H Han, I.S. Lee, K.H. Lee, M.C. Shin, B.B. Choi, Biomed. Mater. Eng. 7 (1997) 253.

2. H.J. Rack, J.I. Qazi, Mater. Sci. Eng. C 26 (2006) 1269.

3. R. Branemark, PI. Branemark, B. Rydevik, RR, Myers, J. Rehabil. Res. Dev. 38 (2001) 175.

4. M. Long, H.J. Rack, Biomaterials 19 (1998) 1621.

5. M.A. Khan, R.L. Williams, D.F. Williams, Biomaterials 20 (1999) 631.

6. M. Niinomi, Mater. Sci. Eng. A243 (1998) 231.

7. H.C. Choe, Thin Solid Films 519 (2011) 4652.

8. Y.H. Jeong, H.C. Choe, W.A. Brantley, I.B. Sohn, Surf. Coat. Technol. 217 (2013) 13.

9. D. Kuroda, M. Niinomi, M. Morinaga, Y. Kato, T. Yashiro, Mater. Sci. Eng. A243 (1998) 244.

10. M. Niinomi, Mettallurgical and Materials Transactions A 33 (2002) 477.

11. H.C. Choe, W.G. Kim, Y.H. Jeong, Surf. Coat. Technol. 205 (2010) S305.

12. K. Das, S. Bose, A. Bandyopadhyay, Acta Biomaterialia 3 (2007) 537.

13. K. Lee, H.C. Choe, B.H. Kim, Y.M. Ko, Surf. Coat. Technol. 205 (2010) S267.

14. Y.H. Jeong, H.C. Choe, W.A. Brantley, Appl. Surf. Sci. 258 (2012) 2129.

15. S. Koutsopoulos, J. Biomed. Mater. Res. 62 (2002) 600.

16. L. Rossi, S. Migliaccio, A. Corsi, M. Marzia, P. Bianco, A. Teti, L. Gambelli, S. Cianfarani, F. Paoletti, F. Branca, J. Nutr. 131 (2001) 1142.

17. T. Wang, J.C. Zhang, Y. Chen, P.G. Xiao, M.S. Yang, J. Trace Elem. Med. Biol. 21 (2007) 84.

18. F. Yang, W.J. Dong, F.M. He, X.X. Wang, S.F. Zhao, G.L. Yang, Oral Surg. Oral Med. Oral Pathol. Oral Radiol. 113 (2012) 313.

19. M. Ikeuchi, A. Ito, Y. Dohi, H. Ohgushi, H. Shimaoka, K. Yonemasu, T. Tateishi, J. Biomed. Mater. Res. A 67 (2003) 1115.

20. R.G. Henning, D.R. Trinkle, J. Bouchet, S.G. Srinvasan, R.C. Albers, J.W. Wilkins, Nature Materials, 4 (2005) 129.

21. P. Robert, Microstructure and Phase transformation of Ti-6Al-4V, (2002)

22. A. Zhecheva, W. Sha, S. Malinov, A. Long, Surf. Coat. Technol. 200 (2005) 2192.

23. S. Shadanbaz, G.J. Dias, Acta biomaterialia 8 (2012) 20.

24. S. Seagle, H. Kessler, in: Principles of Alloying Ti, 3, ASM Battelle Memorial Institute, Columbus, OH, 1968.

25. T. Nishimura, T. Mizoguchi, Y. Itoh, Kobe Res. Dev. 34 (3) (1984) 63.

26. M. Niinomi, Sci. Technol. Adv. Mater. 4 (2003) 445.

27. S.H. Jang, H.C. Choe, Y.M. Ko, W.A. Brantley, Thin Solid Films, 517 (2009) 5038.

28. G. Liu, K. Wang, N. Hoivik, H. Jakobsen, Solar Energy Materials & Solar Cells 98 (2012) 24.

29. G.K. Mor, O.K. Varghese, M. Paulose, K. Shankar, C.A. Grimes, Solar Energy Materials & Solar Cells 90 (2006) 2011.

30. A. Arifin, A.B. Sulong, N. Muhamad, J. Syarif, M.I. Ramli, materials & design 55 (2014) 165.

31. E.J. Kim, W.G. Kim, Y.H. Jeong, H.C. Choe, J. Nanosci. Nanotechnol. 11 (2011) 7433.

32. Y Yang, KH Kim, JL Ong (2005). A review on calcium phosphate coatings produced using a sputtering process-an alternative to plasma sparaying Biomaterials 26 327-337.

33. S. Oh, C. Daraio, L.H. Chen, T.R. Pisanic, R.R. Finones, S. Jin, J. Biomed. Mater. Res. A 78 (2006) 97.

34. M. Uchida, H.M. Kim, T. Kokubo, S. Fujibayshi, T. Nakamura, J. Biomed. Mater. Res. 64 (2003) 164.

35. B. Leon, and J.A. Jansen, Thin Calcoum Phosphate Coatings for Medical Implants, Springer. (2009) 9.

36. D. Shepherd, A volume in woodhead Publising Series in Biomaterials, (2015) 107.

37. S. Roessler, R. Born, D. Scharnweber, H. Worch, A. Sewing, M. Dard, J. Mater. Sci. Mater. Med. 12 (2001) 871.

38. J.J. Park, H.C. Choe, Y.M. Ko, Mat. Sci. Forum 539 (2007) 1270.

39. H.C. Choe, Y.M. Ko, W.A. Brantley, NSTI-Nanotech 2 (2007) 744.

40. A.W. Tan, Pingguan-Murphy, R. Ahmad, S.A. Akbar, Ceram. Int. 38 (2012) 4421.

41. J.H. Schemel, ASTM Manual on Zirconium and Hafnium, ASTM International. 1977.

42. M. Abdel-Hady, H. Fuwa, K. Hinoshita, H. Kimura, Y. Shinzato, M. Morinaga, Scr. Mater. 57 (2007) 1000.

43. A. Pathak, S. Banumathy, R. Sankarasubramanian, A.K. Singh, Computational Mater. Sci. 83 (2014) 222.

44. Y.H. Jeong, H.C. Choe, W.A. Brantley, I.B. Sohn, Surf. Coat. Tech. 271 (2013) 13.

감사의 글

2년 반 동안의 대학원생활을 마무리하면서 지난 치과재료학교실의 생활이 많이 생각납니다. 이러한 생활들은 저에게 인생의 터닝 포인트가 되었습니다. 앞으로 한걸음 더 앞으로 나아가 사회에 있을 때 연구실에서 서로 도와가며 함께 땀을 흘려가며 연구했던 시간들과 경험들이 저에게는 큰 힘이 될 것입니다. 이렇게 저에게 많은 교훈과 뜻 깊은 시간들을 주신 분 들게 감사의 글을 전합니다.

많이 부족한 저에게 아주 소중한 시간과 앞으로 인생에서 사회에서 튼튼한 나무 뿌리처럼 자랄 수 있는 경험과 단단한 바위처럼 빈틈없는 지도를 해 주신 제 인생에 평생 저의 스승님이고 지도교수님이신 최한철 교수님의 잊지 못할 은혜에 고개 숙여 감사드립니다. 또한 바쁘신 가운데도 부족했던 제 논문 심사를 맡아 주시고 꼼꼼히 보시고 많은 조언들을 베풀어 주셨던 손미경 교수님, 김병훈 교수님께도 감사드립니다.

거의 같은 시기에 들어와 같이 실험하며 같이 생활을 하며 실험실원들 중 제일 오래시간을 같이 함께한 김정재 박사님께 감사드립니다. 같이 보냈던 시간과 많은 대화를 하며 많은걸 느끼고 많은 소중한 시간들을 얻게 되어서 감사합니다. 그리고 졸업논문 작성에 있어서 많은 조언과 많은 관심을 주시고 실험에 있어서 노하우와 많은 경험을 주신 이강박사님께 감사드립니다. 졸업하신 김현주 선배님 김성환 선배님 은실이 조채익 선배님 항상 전화나 문자로 조언을 아끼지 않으시고 잘 챙겨주셔서 감사드립니다. 그리고 다른 실험실에서 나와서 치과재료학교실로 잠시 실험을 하러 온 강정인 누나 확고한 목표와 꿈을 위해 달려가면서 따뜻한 마음으로 격려해주셔서 감사합니다. 그리고 박선영 누나 조금이나마 늦게 들어왔지만 빠른 속도로 적응해가며 앞으로의 실험실의 중책을 맡으면서 무리 없이 이끌어 나갈 수 있을 것입니다 그리고 옆에서 많이 도와주셔서 감사합니다. 이제 앞으로 대학원 생활에 접어들 인조와 재인이도 아직 학부생이지만 다른 대학원생들 못지않게 열심히 하는 모습이 너무 좋았습니다. 지난 시간이 얼마 되지 않아서 많은 도움이 되지 못해서 미안해.
마지막으로 하늘에서 보고 수고했다라고 외쳐주시는 존경하는 아버지와 우리아

들 항상 잘 먹고 아프지는 않는지 항상 걱정하고 위로해주시는 어머님께 감사드립니다. 앞으로 자랑스러운 아들이 되겠습니다. 또한 항상 열심히 하고 이제 곧 사회에 접어들 우리 동생 좋은 소식이 있길 응원한다.

<div align="right">

2016.02.

변인섭 올림

</div>

저작물 이용 허락서

학 과	광기술공학과 (광응용공학전공)	학 번	20147138	과 정	석사
성 명	한글: 변 인 섭 한문 : 邊 仁 燮 영문 : In-Seop Byeon				
주 소	전라남도 여수시 안산동 부영아파트 503동 403호				
연락처	E-MAIL : myhottoto@nate.com				
논문제목	한글 : 나노튜브 형성된 Ti-xNb 합금표면에 전기화학적 방법으로 석출된 　　　HA 및 Zn-HA막의 표면특성 영어 : Surface Characteristics of HA and Zn-HA Coatings on the 　　　Nanotubular Ti-xNb Alloys by Electrochemical Deposition Method				

　본인이 저작한 위의 저작물에 대하여 다음과 같은 조건아래 조선대학교가
저작물을 이용할 수 있도록 허락하고 동의합니다.

- 다   음 -

1. 저작물의 DB구축 및 인터넷을 포함한 정보통신망에의 공개를 위한 저작물의
   복제, 기억장치에의 저장, 전송 등을 허락함
2. 위의 목적을 위하여 필요한 범위 내에서의 편집·형식상의 변경을 허락함.
   다만, 저작물의 내용변경은 금지함.
3. 배포·전송된 저작물의 영리적 목적을 위한 복제, 저장, 전송 등은 금지함.
4. 저작물에 대한 이용기간은 5년으로 하고, 기간종료 3개월 이내에 별도의 의사
   표시가 없을 경우에는 저작물의 이용기간을 계속 연장함.
5. 해당 저작물의 저작권을 타인에게 양도하거나 또는 출판을 허락을 하였을
   경우에는 1개월 이내에 대학에 이를 통보함.
6. 조선대학교는 저작물의 이용허락 이후 해당 저작물로 인하여 발생하는 타인에
   의한 권리 침해에 대하여 일체의 법적 책임을 지지 않음
7. 소속대학의 협정기관에 저작물의 제공 및 인터넷 등 정보통신망을 이용한
   저작물의 전송·출력을 허락함.

동의여부 : 동의(O)   반대(   )

2015 년 02 월 25 일

저작자:　　　　　　변 인 섭　　　(서명 또는 인)

조선대학교 총장 귀하